JACS
JOURNAL OF THE AMERICAN CHEMICAL SOCIETY

Article

pubs.acs.org/JACS

Poly(sulfobetaine methacrylate)s as Electrode Modifiers for Inverted Organic Electronics

Hyunbok Lee,[†] Egle Puodziukynaite,[†] Yue Zhang,[†] John C. Stephenson,[‡] Lee J. Richter,[∥] Daniel A. Fischer,[∥] Dean M. DeLongchamp,[∥] Todd Emrick,*[,†] and Alejandro L. Briseno*[,†]

[†]Department of Polymer Science and Engineering, University of Massachusetts, 120 Governors Drive, Amherst, Massachusetts 01003, United States

[‡]Sensor Science Division and [∥]Materials Science and Engineering Division, National Institute of Standards and Technology, 100 Bureau Drive, Gaithersburg, Maryland 20899, United States

Supporting Information

ABSTRACT: We demonstrate the use of poly(sulfobetaine methacrylate) (PSBMA), and its pyrene-containing copolymer, as solution-processable work function reducers for inverted organic electronic devices. A notable feature of PSBMA is its orthogonal solubility relative to solvents typically employed in the processing of organic semiconductors. A strong permanent dipole moment on the sulfobetaine moiety was calculated by density functional theory. PSBMA interlayers reduced the work function of metals, graphene, and poly(3,4-ethylenedioxythiophene):poly(styrenesulfonate) (PEDOT:PSS) by over 1 eV, and an ultrathin interlayer of PSBMA reduced the electron injection barrier between indium tin oxide (ITO) and C_{70} by 0.67 eV. As a result, the performance of organic photovoltaic devices with PSBMA interlayers is significantly improved, and enhanced electron injection is demonstrated in electron-only devices with ITO, PEDOT:PSS, and graphene electrodes. This work makes available a new class of dipole-rich, counterion-free, pH insensitive polymer interlayers with demonstrated effectiveness in inverted devices.

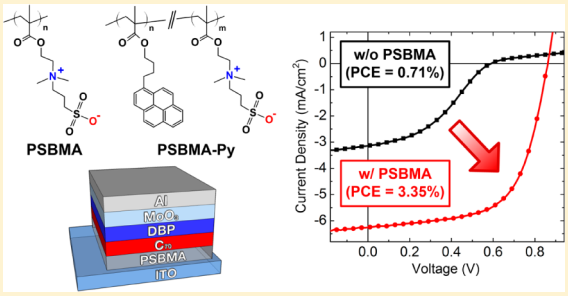

INTRODUCTION

Reducing the charge injection barrier between an electrode and an organic semiconductor is crucial for producing efficient organic electronic devices, since this barrier often dictates device performance.[1,2] Therefore, the ability to easily modify the energy level alignment at the interface between an electrode and an organic semiconductor is of tremendous importance in organic electronic devices. Two established methods for improving charge injection efficiency by controlling the interfacial electronic structures are (1) work function (WF) modification of an electrode by employing an ultrathin layer of a metal oxide or a self-assembled monolayer (SAM)[3−7] and (2) doping of a charge transport layer by electron transfer between dopant and host.[8−10]

Low WF electrodes are of growing interest in organic photovoltaics (OPVs), since it is well-known that inverted OPVs have longer device lifetimes than conventional devices.[11,12] However, there are difficulties in lowering the WF of the cathode for inverted devices, since: (1) alkali metals or alkali earth metals which have low work functions (e.g., Li, K, Ca, Mg, etc.) are unstable in air, and (2) alkali metal halides or alkali earth metal halides (e.g., LiF, CsF, MgF_2, etc.) perform poorly in inverted architectures. In this respect, solution-processable conjugated polyelectrolytes (CPEs) have been found to achieve control over the WF of an electrode.[13−18] CPEs are adaptable to multilayered devices due to their solubility in polar solvents, affording "green" fabrication processes. One attribute of CPEs is that they necessarily incorporate mobile counterions, which are reported to redistribute/diffuse in the charge transport layer. However, such counterions add complexity to understanding charge transfer during device operation, requiring studies devoted to the underlying mechanisms of counterion migration.[19,20] Conjugated polymeric zwitterions (CPZs), dipole-rich polymers free of counterions, also prove useful as interlayers for reducing the WF of metal electrodes. CPZs with sulfobetaine zwitterions greatly improve both OPV devices and organic light-emitting diodes (OLEDs) owing to a reduced WF of the electrode.[21−24] Moreover, Kippelen reported the universal applicability of an aliphatic polyethylenimide ethoxylated (PEIE) interlayer which produces low WF electrodes due to its dipole moment.[25−27]

Inspired by these previous studies, we investigated solution-processable, electronically neutral (counterion free), pH insensitive aliphatic polymer zwitterions as components of inverted devices. Poly(sulfobetaine methacrylate) (PSBMA) can be processed from solvents orthogonal to those used for subsequent organic layer deposition. Its large dipole moment enables control over the WF of a broad range of conventional

Received: November 27, 2014
Published: December 9, 2014

   dx.doi.org/10.1021/ja512148d | J. Am. Chem. Soc. 2015, 137, 540−549

electrodes, including indium tin oxide (ITO), Au, Ag, poly(3,4-ethylenedioxythiophene):poly(styrenesulfonate) (PEDOT:PSS), Cu, and Al. Going further, for modifying the WF of graphene, pyrene-substituted PSBMA copolymers (PSBMA-Py) were utilized.[28] Work function tailoring enables a judicious choice of energy level alignment between electrodes and organic semiconductors in device architectures. This investigation opens a new and simple way to generate low WF electrodes that match the frontier energy levels of a desired electron transport layer and represents a step toward higher efficiency organic electronic devices as a result of improved charge injection.

EXPERIMENTAL SECTION

Density Functional Theory Calculations. The chemical structures of PSBMA and PSBMA-Py (containing about 10 mol % of pyrene methacrylate) are shown in Figure 1 (detailed syntheses in the SI). To investigate the charge distribution of PSBMA and PSBMA-Py, density functional theory (DFT) calculations were conducted with a Becke's 3-parameter exchange and Lee–Yang–Parr correlation (B3LYP) hybrid functional and a 6-31G(d,p) basis set implemented in the Gaussian 09 package.[29−31] For simplicity, one monomer unit of each polymeric zwitterion was calculated as a model system. The geometry was fully relaxed, and the energetic minima was ensured with vibrational frequency analysis.

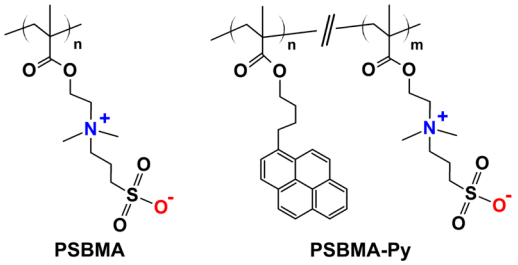

Figure 1. Chemical structures of PSBMA and PSBMA-Py.

Ultraviolet and X-ray Photoelectron Spectroscopy Measurements. Ultraviolet and X-ray photoelectron spectroscopy (UPS and XPS) measurements were carried out on Omicron SPHERA and PHI QUANTUM 2000 ESCA hemispherical spectrometers with He I (21.22 eV) and Al Kα (1486.6 eV) excitation sources, respectively. To obtain the secondary electron cutoff (SEC), a sample bias of −3 V was applied in the normal emission geometry. The base pressure of the analyzer chamber was below 8×10^{-9} mbar. ITO-coated glass was purchased from Thin Film Devices (145 nm, 20 ohms/sq.) and ultrasonically cleaned with deionized (DI) water, detergent, acetone, 2-propanol, methanol, and DI water again. After cleaning, ITO was dried under a N_2 gas flow and used following 15 min of UV-ozone (UVO) treatment or without treatment (bare). For a conducting PEDOT:PSS electrode, the PEDOT:PSS (CLEVIOS PH 1000) film was deposited by spin-casting on UVO-treated ITO at 4000 rpm for 1 min (80 nm) and annealed at 150 °C for 30 min. Metal electrodes were applied to the Si substrate by thermal evaporation (50 nm) in a high-vacuum chamber (<5×10^{-6} mbar). Graphene was synthesized by chemical vapor deposition (CVD) on a Cu foil at 1000 °C, with methane as the carbon precursor. After growth, the graphene was transferred to the Si substrate. PSBMA and PSBMA-Py interlayers were spin-coated onto those electrodes from various solution concentrations (0.05–2.0 mg/mL) at 500 rpm for 5 s and then 4000 rpm for 55 s. The PSBMA and PSBMA-Py solutions in 2,2,2-trifluoroethanol (TFE) were stirred overnight at room temperature and filtered through a PTFE membrane (0.2 μm VWR) prior to deposition. To evaluate the electron injection barrier (EIB) with C_{70}, the C_{70} films (1 and 6 nm) were deposited onto ITO or PSBMA (4 nm)/ITO by thermal evaporation. Samples for UPS and XPS were transferred to the introduction chamber immediately after preparation.

Near-Edge X-ray Absorption Fine Structure Spectroscopy. The carbon K-edge NEXAFS spectra were collected at beamline U7A of the National Synchrotron Light Source of Brookhaven National Laboratory. The spectra were collected in partial electron yield mode with a grid bias of −50 V, providing a surface-weighted signal dominated by the outermost (2–4 nm) portion of the film, i.e., the material in contact with C_{70}. Several incident angles were employed to vary the angle of the electric field vector with respect to sample normal. Data shown are normalized to the post-edge intensity at 330 eV, to eliminate intensity variations due to different spot size at different angles.

Vibrationally Resonant Sum Frequency Generation Spectroscopy. Vibrationally resonant sum frequency generation (VR-SFG) spectra were acquired from PSBMA films on Au substrates with a custom built, broad bandwidth system. In brief, a Ti-sapphire regenerative amplifier system, generating 12 W of nominally 100 fs duration pulses at 3 kHz repetition rate was used to simultaneously pump two optical parametric amplifier (OPA) systems. In one system, a near-infrared (IR) OPA generated sub 100 fs pulses at ≈ (1470 and 1750) nm that were sent to a noncollinear difference frequency generator to produce ≈5 μJ, ≈ 150 cm^{-1} bandwidth, IR pulses centered at ≈1100 cm^{-1}. In the second system, a second harmonic bandwidth compressor was used to produce ≈3 cm^{-1}, 400 nm center wavelength pulses that pumped an OPA resulting in tunable 8 cm^{-1} bandwidth pulses centered at 785 nm. SSP SFG spectra (s-polarized sum frequency, s-polarized 785 nm, p-polarized IR) were acquired with the 785 nm and IR incident on the sample at 35.8° and 54.2°, respectively. The visible pulse was incident at a slight (1.3 ps) delay with respect to the IR pulse, to maximize the heterodyne between the Au substrate and the film. The sample signal was normalized to the signal from a Au substrate, coated with an octanedithiol SAM.

In the SSP configuration, the SFG signal (for a single resonance) can be expressed as

$$\text{signal} = \left| \chi^{e}_{nr} + \frac{\chi^{e}_{r} e^{i\phi}}{\upsilon - \upsilon_0 - I\Gamma} \right|^2$$

where χ^{e}_{nr} is the effective, nonresonant susceptibility, dominated by the Au substrate, and χ^{e}_{r} is the resonant susceptibility, arising from the A_1 symmetric stretch of the C_{3v} SO_3^-. χ^{e}_{r} is given by the xxz element of the averaged molecular hyperpolarizability β:

$$\chi^{e}_{xxz} = \int dz F_{lx}(\nu_{sum}, z) F_{mx}(\upsilon_{vis}, z) F_{nz}(\upsilon_{IR}, z) \iiint \sin\theta d\theta d\phi d\psi \beta_{ijk} R_{il} R_{jm} R_{kn} f(\theta, \phi, \psi, z)$$

where F_{lx} is the relevant Fresnel factor (including local field corrections), R_{il} is a standard rotation matrix, and $f(\theta,\phi,\psi,z)$ is the depth-dependent, normalized orientation distribution. The magnitude of the product of the three Fresnel factors as a function of distance from the film/Au interface for a 4 nm film thickness is shown in Figure S5. The depth average slightly favors the air/film interface, due to strong screening of the in-plane fields by the metal.

Organic Photovoltaic and Electron-Only Device Fabrication. ITO-coated glass substrates were cleaned, and the PSBMA interlayer was spun-cast as described above. 40 nm-thick C_{70} (American Dye Source, purity >99%) films and 15 nm-thick tetraphenyldibenzoperiflanthene (DBP, Sigma-Aldrich, purity 98%) films were thermally evaporated sequentially on ITO or PSBMA (0–16 nm)/ITO as acceptor and donor layers, respectively, with a deposition rate of 0.1 nm/s. The DBP was purified by vacuum sublimation in a horizontal furnace with a thermal gradient prior to use, while C_{70} was used as received. Device fabrication was completed by depositing MoO_3 (10 nm) at a deposition rate of 0.01 nm/s and Al (100 nm) with a deposition rate of 0.01–0.1 nm/s for the bilayer anode. Thermal evaporations were conducted in a high-vacuum chamber with a rotating sample holder. Both deposition rate and total thickness were monitored with a quartz crystal microbalance (QCM). The devices were annealed at 100 °C for 30 min under a N_2 atmosphere. For electron-only devices, a C_{60} (200 nm, Puyang Huicheng Chemical Co., purity 99%) electron transport layer was deposited onto ITO or PSBMA (4 nm)/ITO in

dx.doi.org/10.1021/ja512148d | J. Am. Chem. Soc. 2015, 137, 540–549

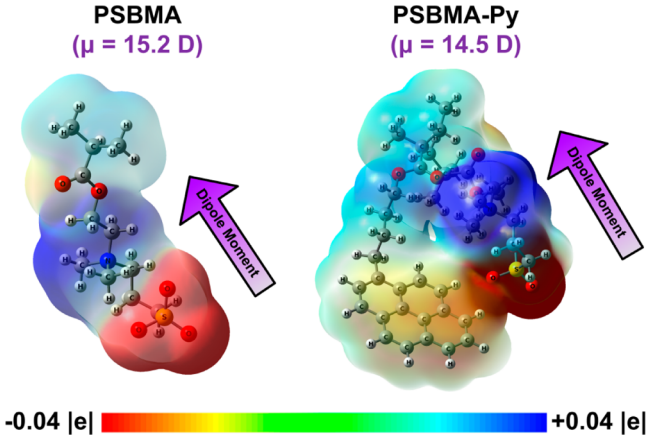

Figure 2. Graphical charge distributions for one monomer unit of PSBMA and PSBMA-Py from DFT calculations.

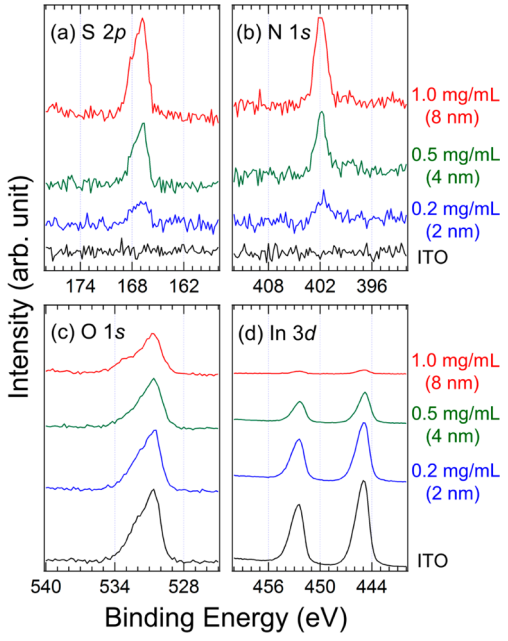

Figure 3. XPS spectra of (a) S 2p, (b) N 1s, (c) O 1s, and (d) In 3d of the PSBMA interlayer on an ITO electrode with varying the thickness from different solution concentrations (0.2, 0.5, and 1.0 mg/mL).

the same manner. After C_{60} deposition, Ca (10 nm) and Al (100 nm) bilayer cathodes were deposited. PEDOT:PSS and graphene electrodes were prepared on glass substrates. Current density−voltage (J–V) characteristics were measured with a Keithley 4200-SCS parameter analyzer under AM1.5 condition with a 100 mW/cm^2 illumination using a solar simulator (Newport) calibrated using a Si reference solar cell.

Atomic Force Microscope Measurements. To investigate surface morphology, atomic force microscopy (AFM) measurements were conducted on ITO, PSBMA (4 nm)/ITO, C_{70} (40 nm)/ITO, and C_{70} (40 nm)/PSBMA(4 nm)/ITO. All of those samples were prepared in the same manner as for device fabrication. AFM topography images were obtained using a Digital Instruments Dimension 3000 scanning force microscope in the tapping mode.

RESULTS AND DISCUSSION

Dipole Moment of Polymeric Zwitterions from DFT Calculations. Figure 2 shows the graphical charge distribution of one monomer unit of PSBMA and PSBMA-Py resulting from DFT calculations, with SO_3^- as the negatively charged

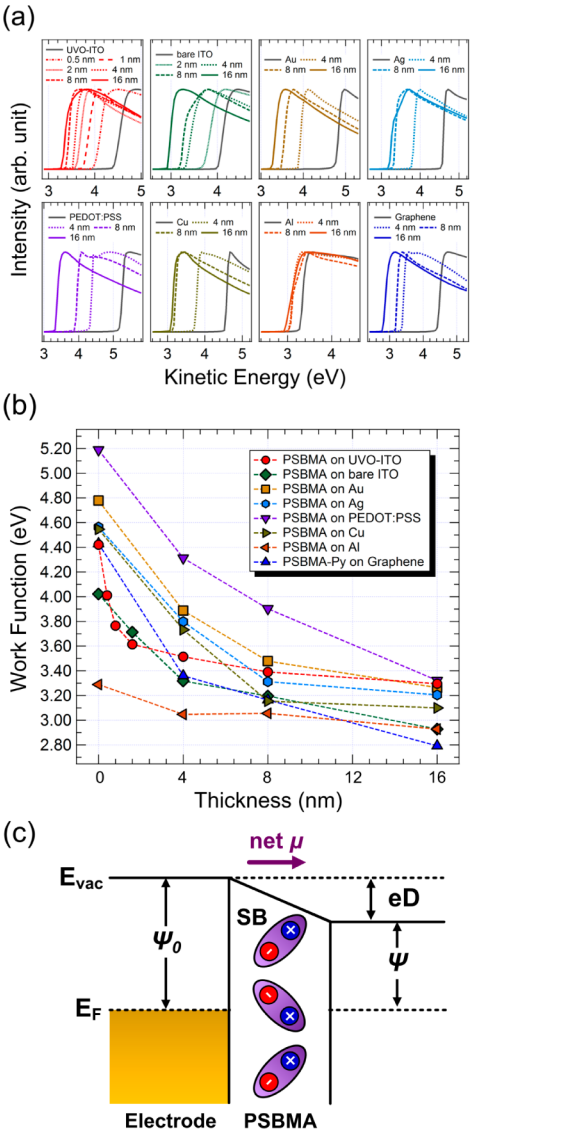

Figure 4. (a) UPS spectra of the secondary electron cutoff (SEC) region of the PSBMA interlayer (0−16 nm) on UVO-treated ITO, bare ITO, Au, Ag, PEDOT:PSS (PH1000), Cu, Al, and the PSBMA-Py interlayer on graphene. (b) Change in WF with interlayer thickness. (c) Representation of PSBMA-induced interface dipole.

groups (red) and N^+ as the positively charged groups (blue). The calculated dipole moment of PSBMA was 15.2 D and that of PSBMA-Py was 14.5 D. The dipole moment arises from the zwitterionic sulfobetaine, with little contribution from the pyrene moiety for PSBMA-Py. Such large dipole moments can contribute to an interface dipole (eD) when the polymers are associated with conductive materials, which lowers the WF of the conductor.[1] The optimized geometries and full Mulliken atomic charges are shown in Figure S1 and Table S1 (see SI).

Thickness Estimation with XPS Core Level Spectra. Figure 3 shows the XPS core level spectra of (a) S 2p, (b) N 1s, (c) O 1s, and (d) In 3d of the PSBMA interlayer on ITO-coated glass at varying concentrations of polymer solution used for spin-coating (0.2, 0.5, and 1.0 mg/mL). In Figure 3a−c, the photoelectron spectrum intensities of S 2p at 166.8 eV, N 1s at 402.0 eV, and O 1s at 533.2 eV, which originate from PSBMA, evolve with increasing concentration of the cast solution, indicating a good correlation between polymer film thickness with solution concentration. While the thickness of a conventional

dx.doi.org/10.1021/ja512148d | J. Am. Chem. Soc. 2015, 137, 540−549

Table 1. Work Function of Wide-Ranging Electrodes with Varying Thickness of the PSBMA Interlayer (UVO-treated ITO, bare ITO, Au, Ag, PEDOT:PSS, Cu, and Al) and the PSBMA-Py Interlayer (graphene)

thickness (nm)	UVO-treated ITO	bare ITO	Au	Ag	PEDOT:PSS (PH 1000)	Cu	Al	graphene
0	4.42	4.02	4.78	4.56	5.19	4.55	3.29	4.43
2	3.61	3.71	–	–	–	–	–	–
4	3.51	3.32	3.89	3.80	4.31	3.73	3.05	3.36
8	3.39	3.20	3.48	3.31	3.90	3.15	3.06	3.16
16	3.30	2.93	3.26	3.21	3.32	3.10	2.93	2.79

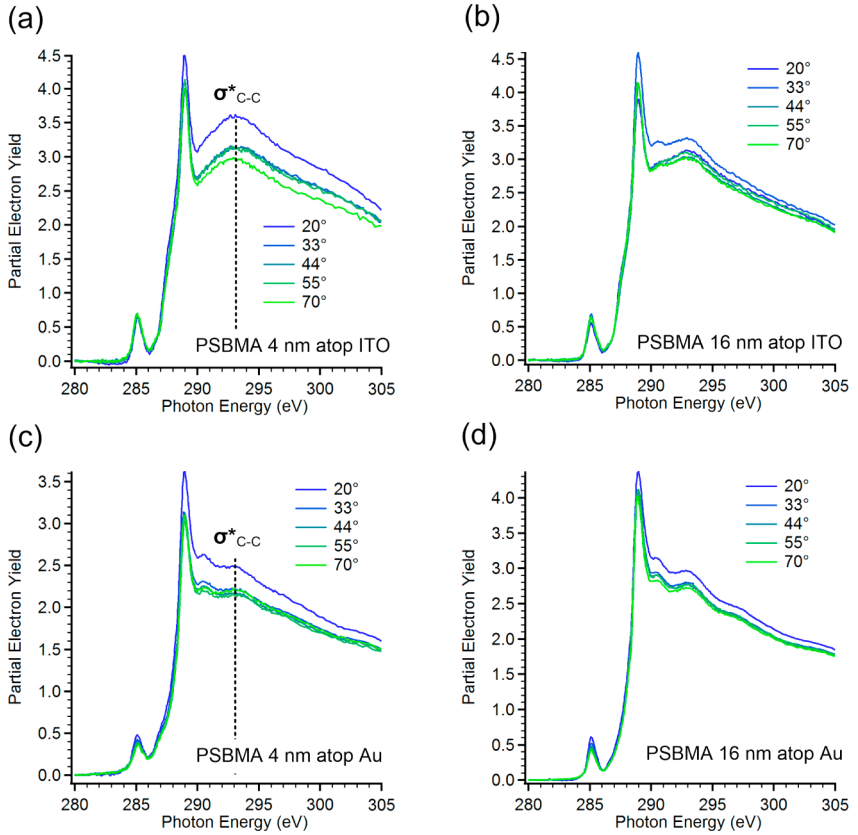

Figure 5. Carbon K-edge NEXAFS spectra of (a) a 4 nm-thick PSBMA film on ITO, (b) a 16 nm-thick PSBMA film on ITO, (c) a 4 nm-thick PSBMA film on Au, and (d) a 16 nm-thick PSBMA film on Au.

polymer layer is measured reliably with a stylus-based surface profiler, the ultrathin nature of the PSBMA and PSBMA-Py films required XPS to estimate the thickness, using the intensity attenuation of the substrate core level spectrum and the following equation:

$$I = I_0 \exp\left(-\frac{d}{\lambda \sin \varphi}\right)$$

where I is the In $3d_{5/2}$ photoelectron spectrum intensity attenuated by the PSBMA upper layer, I_0 is the In $3d_{5/2}$ photoelectron spectrum intensity of bare ITO, d is the PSBMA interlayer thickness, λ is the attenuation length, and φ is the XPS takeoff angle (45° in our measurements). This method is frequently used for ultrathin films, such as SAMs, and agrees with ellipsometry results.[32,33] The binding energy of In $3d_{5/2}$ was measured as 444.8 eV (i.e., kinetic energy of 1041.8 eV) and its λ was estimated to be 3 nm from the reported value of poly(methyl methacrylate) (PMMA) (the backbone structure of PSBMA).[34] Thus, the thickness of PSBMA interlayers obtained from different solution concentrations are 0.2 mg/mL = 2 nm; 0.5 mg/mL = 4 nm; and 1.0 mg/mL = 8 nm. We assume that PSBMA-Py solutions of similar concentrations to those of PSBMA give films of similar thickness.

Work Function Reduction with Polymeric Zwitterion Coatings. Figure 4a shows the normalized UPS spectra of the SEC region with varying thickness of PSBMA or PSBMA-Py layers on UVO-treated ITO (WF = 4.42 eV), bare ITO (WF = 4.02 eV), Au (WF = 4.78 eV), Ag (WF = 4.56 eV), conducting PEDOT:PSS (WF = 5.19 eV), Cu (WF = 4.55 eV), Al (WF = 3.29 eV), and graphene (WF = 4.43 eV). All of the electrodes are expected to have a native oxide layer due to air exposure. Notably, the WF of all of the electrodes is reduced following deposition of the polymeric zwitterion film. With increasing film thickness, the electrode WF is reduced, and at 16 nm thickness the WFs of the electrodes are reduced by more than 1 eV: 1.12 eV for UVO-treated ITO, 1.09 eV for bare ITO, 1.52 eV for Au, 1.35 eV for Ag, 1.87 eV for PEDOT:PSS, 1.45 eV for Cu, and 1.64 eV for graphene. The AlO_x layer on Al already induces a low WF, and thus the small observed WF reduction (0.36 eV) was expected. WF values observed as a function of polymer thickness are summarized in Figure 4b and Table 1. The WFs are steeply reduced to around 3.4-to-3.6 eV,

dx.doi.org/10.1021/ja512148d | J. Am. Chem. Soc. 2015, 137, 540−549

and the reduction thereafter becomes less pronounced. With polymeric zwitterion films greater than 16 nm, strong charging effects were observed in the photoelectron spectra (not shown) due to the insulating character of PSBMA and PSBMA-Py. Therefore, in devices, these polymers will be best applied as ultrathin films. Based on the WF reduction, we hypothesize that the eD, which modifies the surface electronic structure, is directed as illustrated in Figure 4c. Positive eD formation of the polymeric zwitterion interlayers could in principle originate from (1) the push-back effect from Pauli repulsion by polymeric adsorbates and (2) the permanent dipole moment associated with the zwitterionic pendent groups.[1,2] Conjugated polymer interlayers without zwitterionic chains moderately reduce the WF of an electrode via the push-back effect (0.61, 0.79 eV), while CPZs significantly reduce WF (0.84, 0.96 eV).[22] Similarly, we observed that PMMA interlayers (having the same backbone as PSBMA and PSBMA-Py, but without zwitterionic chains) show moderate WF change on UVO-treated ITO substrates (Figure S2), attributed to a very small dipole moment on PMMA (calculated μ = 1.7 D). This molecular dipole-induced eD model is similarly suggested in polymeric WF modifiers, such as CPEs and polyethylenimines.[25,35−37]

Zwitterion Chain Orientation Measurements with NEXAFS. The surface-relative orientation of the zwitterionic moiety is of critical importance if its dipole is expected to influence the WF. To measure this orientation, we apply surface-sensitive NEXAFS spectroscopy,[38] which is a robust tool for determining the average bond orientation in thin layers of organic molecules, particularly when applied at the carbon K-edge. NEXAFS has been used to determine alkane side chain orientation on organic semiconductors,[39] and, more classically, in alkane SAMs.[40] NEXAFS spectra of PSBMA on ITO and Au are shown in Figure 5. The peak at ≈285 eV is the 1s → π^* of typical adventitious aromatic hydrocarbon contamination. The peak at ≈289 eV is likely a convolution of carbon−hydrogen 1s → σ^*, carbon−sulfur 1s → σ^*, and Rydberg excitations. The most dominant peak at ≈293 eV is consistent with carbon−carbon 1s → σ^*. This carbon−carbon 1s → σ^* exhibits variable intensity with incident angle; the lowest intensity is for near-normal incidence, where the electric field vector of incident soft X-rays is nearly parallel to the substrate plane and the highest intensity is for the shallowest incidence where the electric field vector is nearly perpendicular to the substrate plane. Because the 1s → σ^* transition dipole moment runs parallel to the σ bond, the angular dichroism is consistent with a net carbon−carbon bond orientation preference perpendicular to the substrate plane. Because the side chain carbon−carbon bonds significantly outnumber the backbone carbon−carbon bonds, the orientation of this feature will be determined by side chain behavior. We can therefore conclude that the side chains, and therefore the zwitterionic moieties, have a net orientation perpendicular to the substrate plane, though likely not perfectly vertical. The extent of dichroism is relatively modest compared to that of a well-packed alkane SAM, which is illustrated in Figure S3 (note, however, the similar angular dependence of the peak at 293 eV). The side chain orientation is likely widely distributed, with a first moment having a modest preference for vertical. A similar orientation was observed across PSBMA samples of varied thickness on several substrates, although 4 nm PSBMA films are less consistently oriented which might be attributed to some extent of heterogeneous polymer distribution spot-to-spot orientational heterogeneity. NEXAFS cannot determine the dipole sign, i.e., whether it is pointing "up" or "down," but it does indicate some degree of side chain orientation preference consistent with our hypothesis that the dipole is oriented as depicted in Figure 4c. Given the considerable molecular dipole moment (∼15 D), the "net" dipole moment that is perpendicular to the electrodes affecting the WF could be large enough although the orientation is modest. The driving force for orientation can be described in an electrostatic model of an image dipole induced by surface polarization.[22] This electrostatic force influences polymeric assembly and dipole orientation, which leads to a positive net dipole moment, and the corresponding WF reduction.

Dipole Sign Determination by VR-SFG. To determine the dipole sign, VR-SFG spectra were acquired on the SO_3 anion in PSBMA films on Au substrates and are reported in Figure 6. Linear techniques, such as NEXAFS, determine

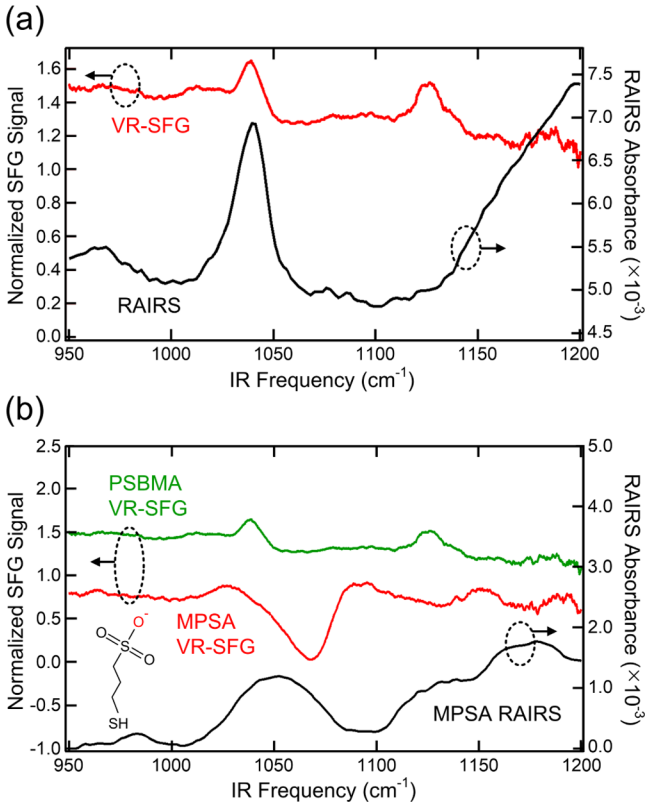

Figure 6. SSP VR-SFG spectra of the SO_3 functional group of a 4 nm-thick PSBMA fim on Au (a) and comparison to that of a MPSA SAM assembled on Au (b). RAIRS spectra and the molecular structure of MPSA are also shown.

$\langle\cos^2\theta\rangle$, where θ is the orientation angle of the transition dipole with respect to the surface, and thus can only determine alignment. Second-order nonlinear techniques, such as SFG, determine $\langle\cos^3\theta\rangle$ and can thus measure orientation, i.e., the total vector direction of the relevant functional group. The vector nature of SFG implies that the signal is null for isotropically distributed chromophores. Shown in Figure 6a is a reflection−absorption IR spectrum (RAIRS) of a 16 nm PSBMA film and the VR-SFG spectrum of a 4 nm film. The A_1 stretch of the SO_3 is clearly visible as a constructive interference feature at ≈1040 cm^{-1}. The feature at 1125 cm^{-1} is likely the asymmetric stretch and is often weak in IR spectra. In order to calibrate the relative phase between the SO_3 hyperpolarizability and the nonresonant background of the Au, we acquired SSP, VR-SFG

dx.doi.org/10.1021/ja512148d | J. Am. Chem. Soc. 2015, 137, 540−549

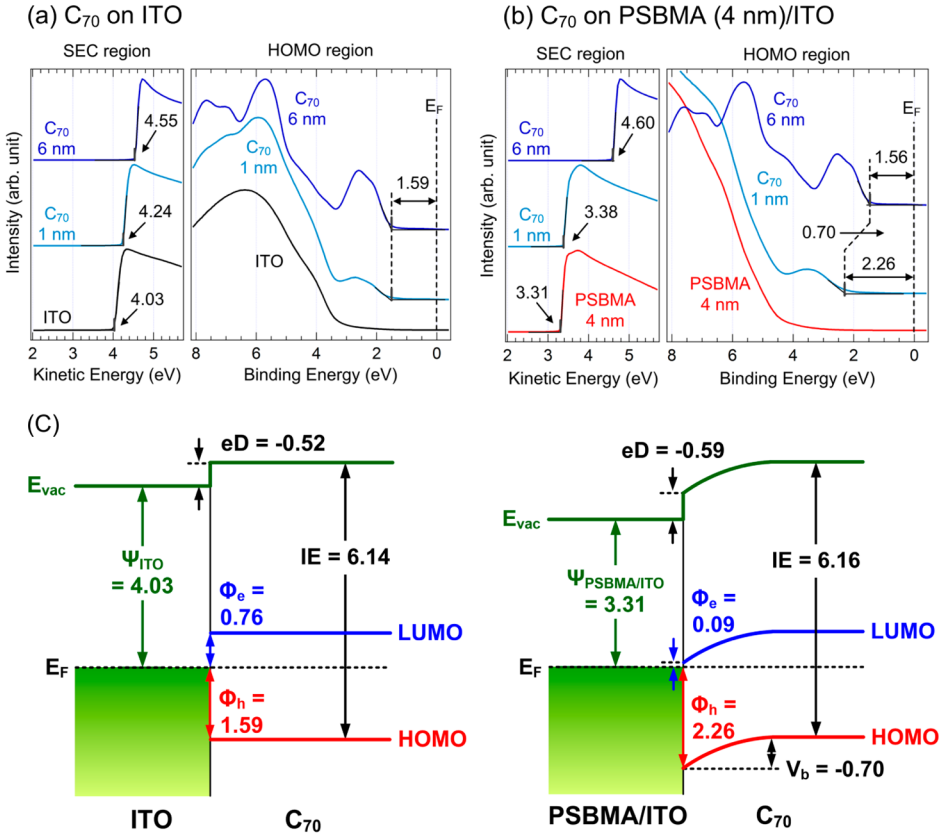

Figure 7. UPS spectra of (a) C_{70} (1, 6 nm)/ITO and (b) C_{70} (1, 6 nm)/PSBMA (4 nm)/ITO. (c) Energy level diagrams of C_{70}/ITO and C_{70}/PSBMA/ITO. Ψ, IE, Φ_h, Φ_e, eD, and V_b denote the work function, ionization energy, hole injection barrier, electron injection barrier, interface dipole, and band bending, respectively.

spectra under identical conditions of a reference SAM of 1-mercapto-3-isopropyl sulfonate (MPSA), formed by immersion of a ultraviolet ozone cleaned, evaporated Au film in a 270 μmol/L solution of MPSA in 30 mmol/L perchloric acid (Figure 6b). The MPSA SAM exhibits significantly broadened features in both the VR-SFG and RAIRS. Since it is the thiol sulfur chemisorbing to Au, the SO_3 anion must point away from the Au surface.[41] There is clear destructive interference between the MPSA SO_3 and the Au background. Thus, we can conclude that the net orientation of the SO_3 in the PSBMA is the opposite, i.e., that the SO_3 groups point, on average, toward the Au. The absence of significant structure in the E SO_3 region of the MPSA spectrum suggests that the SO_3 is essentially normal to the surface in the SAM. The relatively weak spectrum of the PSBMA suggests that, on average, the density of oriented SO_3 in the polymer film is less than a typical thiol monolayer density of $\approx 4 \times 10^{14}$ cm^{-2}. For films as thin as those characterized here, the signal is essentially the net orientation of the chromophore throughout the entire film (the interference structure of the electric fields results in an average slightly biased toward the air interface, see Figure S5) and thus should directly relate to the WF change. From the sign of the interference between the SO_3^- signal and the Au background, it is clear that the net orientation of the C−SO_3^- director is with the SO_3^- pointing toward the Au, as indicated in Figure 4c. This supports the attribution of the WF change to partial alignment of the permanent dipoles of the PSBMA side groups.

Reduced Electron Injection Barrier (EIB). Accurate knowledge of the EIB of organic semiconductors is of key importance since the vacuum level is often misaligned due to the eD between the electrode and organic semiconductor.[42,43] Therefore, the energy level alignment of C_{70} on ITO and PSBMA on ITO was investigated by UPS, as shown in Figure 7a,b for the SEC and HOMO regions of C_{70} (1, 6 nm)/ITO and C_{70} (1, 6 nm)/PSBMA (4 nm)/ITO. The SEC region spectra were normalized and plotted as kinetic energies, such that the data correspond directly to WF. A Shirley-type of background from inelastic scattering of photoelectrons was removed from the measured HOMO region of the spectrum. In Figure 7a, the WF of bare ITO was measured at 4.03 eV. With a 1 nm-thick deposition of the C_{70} layer, the HOMO onset of C_{70} was observed at 1.59 eV from the Fermi level and did not shift at 6 nm thickness, indicating an absence of band bending (V_b) effects in the C_{70} layer. The SEC gradually shifts toward higher kinetic energies with C_{70} deposition and is observed at 4.55 eV for a 6 nm film. In Figure 7b, the WF of ITO is reduced to 3.31 eV with a 4 nm-thick PSBMA layer, which reproduces the WF shown in Table 1. With a 1 nm-thick C_{70} layer, the HOMO onset of C_{70} is observed at 2.26 eV, shifting toward lower binding energies by 0.70 eV at 6 nm thickness. The SEC shifts slightly (by 0.07 eV) toward higher kinetic energies for a 1 nm-thick C_{70} film and shifts significantly (by 1.22 eV) for a 6 nm film. The energy level diagrams of C_{70}/ITO and C_{70}/PSBMA/ITO in Figure 7c show that the ionization energies (IEs) for both C_{70} on ITO and PSBMA/ITO are the same within margin-of-error (6.14 and 6.16 eV), indicating that their morphologies are unchanged by the PSBMA interlayer.[6,44−46] The total work function change ($\Delta\Psi$) for thermal equilibrium can be expressed by

$$\Delta\Psi = -(\mathrm{eD} + V_b)$$

dx.doi.org/10.1021/ja512148d | J. Am. Chem. Soc. 2015, 137, 540−549

where eD is the interface dipole and V_b is the band bending which can be evaluated from the HOMO onset shift during C_{70} deposition.[47,48] By this evaluation, the eD at the interface between C_{70} and ITO is −0.52 eV (V_b = 0). On the other hand, the eD is −0.59 eV and V_b is −0.70 eV at the interface between C_{70} and PSBMA/ITO, respectively. This large V_b was similarly observed in the C_{60} layer on another low WF electrode (NaCl/Ag), which would arise from the lower WF of the electrode relative to the electron affinity (EA) of the contacted organic semiconductor leading to charge transfer.[49] The EIB for each interface is estimated by the reported transport energy gap of C_{70} (2.35 eV).[50] As a result, the EIB between C_{70} and ITO is reduced dramatically, from 0.76 to 0.09 eV, by inserting the PSBMA interlayer. Such a reduction in EIB will significantly improve organic electronic device performance.

OPV Performance with Enhanced Electron Injection. Inverted OPVs were fabricated with a small molecule bilayer heterojunction. Such bilayer OPVs represent suitable model devices to demonstrate enhanced device performance without complicating external factors. Figure 8a shows an inverted

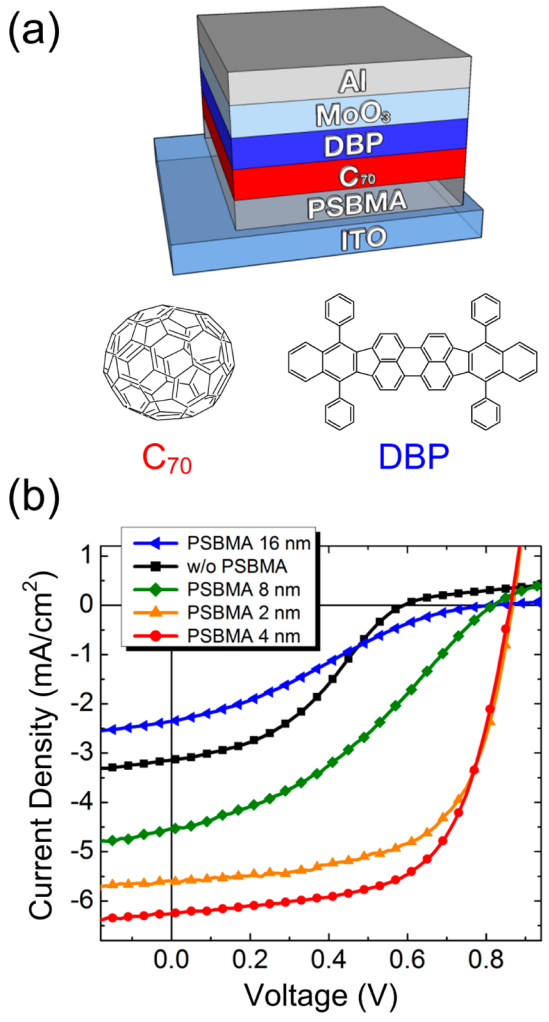

Figure 8. (a) Device configuration of inverted OPVs which consist of Al (100 nm)/MoO_3 (10 nm)/DBP (15 nm)/C_{70} (40 nm)/PSBMA (0, 2, 4, 8, and 16 nm)/ITO. (b) J–V characteristics with varying the thickness of the PSBMA interlayer upon illumination.

device structure containing C_{70} and DBP, and Figure 8b shows the measured J–V characteristics upon illumination (J–V characteristics with varying post-annealing time are given in the SI). Without the PSBMA interlayers, an S-shaped kink near the open circuit voltage (V_{OC}) is observed, resulting from the large EIB (0.76 eV) between C_{70} and ITO, and the small WF difference between the anode and cathode.[51] As a result, device performance is poor [short circuit current (J_{SC}) = 3.14 mA/cm^2, V_{OC} = 0.60 V, fill factor (FF) = 0.38, and power conversion efficiency (PCE) = 0.71%]. However, the presence of a PSBMA interlayer removes the S-shaped kink due to the significantly reduced EIB (0.09 eV) and the large WF difference between the electrodes, and all OPV parameters improve dramatically (detailed values are summarized in Table 2). The best

Table 2. OPV Parameters of Inverted OPVs with Varying Thickness of PSBMA Interlayers for Best Performing Devices

thickness (nm)	J_{SC} (mA/cm^2)	V_{OC} (V)	FF	PCE (%)
0	3.14	0.60	0.38	0.71
2	5.60	0.87	0.62	3.01
4	6.25	0.87	0.62	3.35
8	4.53	0.82	0.35	1.31
16	2.36	0.82	0.25	0.48

performing device contained a 4 nm-thick PSBMA interlayer (J_{SC} = 6.25 mA/cm^2, V_{OC} = 0.87 V, FF = 0.62, and PCE = 3.35%), while thicker interlayers led to diminished performance due to the insulating nature of the polymer backbone. Thus, although electrodes with interlayers thicker than 4 nm show a lower WF (Figure 4), an increased series resistance impacts device performance. In addition, the LUMO level of most n-type organic semiconductors (C_{70} in this instance) would be held constant with such a low WF electrode, prepared from 4 nm-thick PSBMA and PSBMA-Py layers, and optimized device performance would be expected when using ultrathin films. J–V characteristics for devices utilizing an 8 nm PSBMA interlayer show the return of the S-shaped kink due to charge accumulation at the interface between C_{70} and PSBMA/ITO (J_{SC} = 4.53 mA/cm^2, V_{OC} = 0.82 V, FF = 0.35, and PCE = 1.31%). Finally, the PCE of an OPV fabricated with a 16 nm PSBMA interlayer (J_{SC} = 2.36 mA/cm^2, V_{OC} = 0.82 V, FF = 0.25, and PCE = 0.48%) is lower than that without the PSBMA interlayer. A significant enhancement of device performance is similarly observed in inverted OPVs with both polymer bulk heterojunction (P3HT:$PC_{61}BM$) on PSBMA/ITO and bilayer heterojunction on PSBMA-Py/graphene (i.e., no ITO) electrode on the glass substrate (SI).

Surface Morphologies characterized by AFM. Figure 9 shows topographic images of (a) ITO, (b) PSBMA (4 nm)/ITO, (c) C_{70} (40 nm)/ITO, and (d) C_{70} (40 nm)/PSBMA (4 nm)/ITO. Figure 9a,b indicates that the PSBMA interlayer covers most of the ITO. However, small voids are present on the PSBMA film, and a surface profile indicates a height difference of 4 ± 1 nm, in good agreement with the XPS-estimated thickness (Figure 3). We also determined the morphology of C_{70} with and without the PSBMA interlayer, which can affect V_{OC} due to intermolecular coupling, and J_{SC} due to the interfacial area between the donor and acceptor layers.[52,53] The RMS roughness of C_{70}/ITO is ∼0.38 nm, and that of C_{70}/PSBMA/ITO is ∼0.55 nm, indicating no significant change disruption introduced by the PSBMA interlayer. Therefore, device improvements are reasonably attributed to a favorable

dx.doi.org/10.1021/ja512148d | J. Am. Chem. Soc. 2015, 137, 540−549

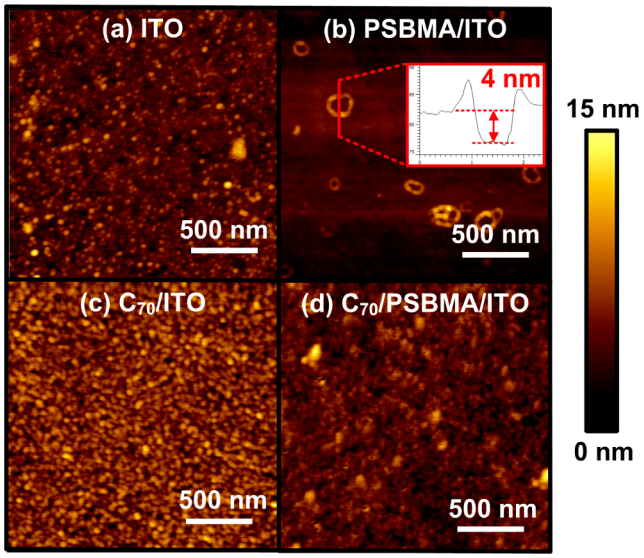

Figure 9. AFM topography images of (a) ITO, (b) PSBMA (4 nm)/ITO, (c) C_{70} (40 nm)/ITO, and (d) C_{70} (40 nm)/PSBMA (4 nm)/ITO (scale bar = 500 nm). Inset of (b) shows a surface profile anaylsis of the PSBMA interlayer, which displays the height difference is 4 ± 1 nm. The RMS roughnesses are (c) C_{70} on ITO (~0.38 nm) and (d) on PSBMA/ITO (~0.55 nm), respectively.

energy level alignment between C_{70} and ITO enabled by the polymeric zwitterion interlayers.

Electron-Only Devices with ITO, PEDOT:PSS, and Graphene. The transparency of PSBMA and PSBMA-Py interlayers allows their effective use with transparent electrodes in optoelectronic devices (transmittance spectra shown in SI). To demonstrate the enhanced electron injection efficiency with the transparent electrodes, electron-only devices were fabricated with ITO, PEDOT:PSS, and graphene electrodes. Figure 10a,b shows the device configuration and the measured $J-V$ characteristics on a log–log scale, respectively. With the PSBMA interlayer on ITO, the J at 6 V is >3 orders larger than that without the PSBMA interlayer. The significantly improved and virtually linear $J-V$ characteristics with the PSBMA interlayer indicate a negligible EIB at the interface between ITO and C_{60}, whereas the $J-V$ characteristics without PSBMA interler are injection limited.[54,55] In the case of PEDOT:PSS, the increase in J at 6 V is much less, which might originate from the intrinsic lower conductivity and relatively higher WF of a PEDOT:PSS electrode relative to ITO. With the PSBMA-Py interlayer on graphene, the J at 6 V is >2 orders larger than that without the PSBMA-Py interlayer. These results confirm that the origin of the enhanced OPV performance is the greatly improved electron injection efficiency and also suggest the potential application of polyzwitterion interlayers with transparent electrodes in optoelectronic devices.

CONCLUSION

We demonstrate the application of new solution-processable and counterion-free polymeric zwitterion interlayers in the form of the zwitterionic methacrylate polymers PSBMA and PSBMA-Py. PSBMA and PSBMA-Py interlayers strongly reduce the WF of electrodes by more than 1 eV, originating from an eD on the electrodes. This reduced WF induces a large V_b in the C_{70} layer and a significantly reduced EIB between ITO and C_{70}. These favorable electronic properties were exploited in inverted OPVs and electron-only devices. In OPVs, the polymeric zwitterions removed S-shaped kinks in $J-V$ curves, and all device metrics were enhanced significantly when the interlayer was employed. In simple electron-only devices, larger J values were observed owing to an enhanced charge injection efficiency with polymeric zwitterion interlayers. Thus, these polymeric zwitterions may be widely applicable to numerous types of electronic devices requiring a low WF electrode.

ASSOCIATED CONTENT

Supporting Information

Detailed synthetic steps of PSBMA and PSBMA-Py, Cartesian coordinates of optimized structures and full Mulliken atomic charge analysis from DFT calculations, WF change on UVO-ITO with the PMMA layer, NEXAFS spectra of OTS SAM, computed Fresnel factor product of PSBMA/Au, full UPS spectrum of PSBMA/UVO-ITO and PSBMA-Py/graphene, annealing effects on OPVs, $J-V$ characteristics of inverted polymer OPVs with the PSBMA interlayer and bilayer OPVs with the graphene electrode and transmittance spectra. This material is available free of charge via the Internet at http://pubs.acs.org.

AUTHOR INFORMATION

Corresponding Authors

abriseno@mail.pse.umass.edu
tsemrick@mail.pse.umass.edu

Notes

The authors declare no competing financial interest.

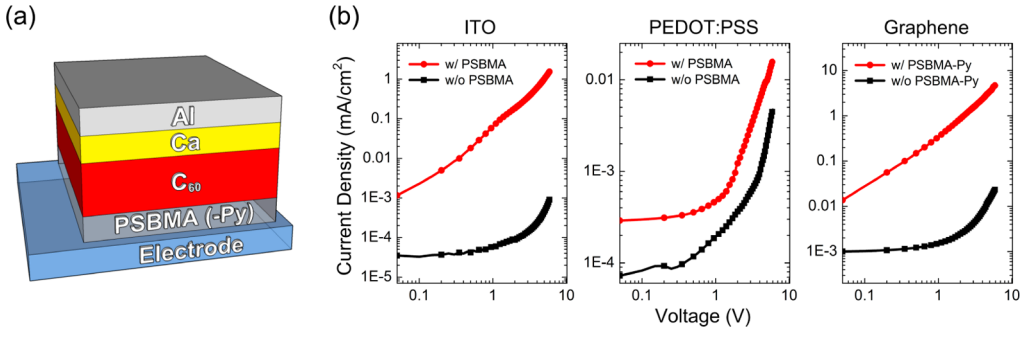

Figure 10. (a) Configuration of electron-only devices which consist of Al (100 nm)/Ca (10 nm)/C_{60} (200 nm)/PSBMA (0 and 4 nm)/ITO or PEDOT:PSS on a glass substrate and Al (100 nm)/Ca (10 nm)/C_{60} (200 nm)/PSBMA-Py (0 and 4 nm)/graphene on a glass substrate and (b) the respective measured $J-V$ characteristics.

dx.doi.org/10.1021/ja512148d | J. Am. Chem. Soc. 2015, 137, 540–549

■ ACKNOWLEDGMENTS

H. L, Y. Z., and A.L.B acknowledge the support of the Office of Naval Research (N000141110636, N0001471410053) and the National Science Foundation for support (DMR-1112455). T.E. acknowledges the support of NSF-CHE 1152360 for polymer synthesis and surface functionalization. UPS measurements were carried out in the Polymer-Based Materials for Harvesting Solar Energy Laboratory, an Energy Frontier Research Center funded by the U.S. Department of Energy, Office of Basic Energy Sciences under award number DE-SC0001087.

■ REFERENCES

(1) Ishii, H.; Sugiyama, K.; Ito, E.; Seki, K. *Adv. Mater.* **1999**, *11*, 605−625.
(2) Koch, N. *ChemPhysChem* **2007**, *8*, 1438−1455.
(3) Lee, H.; Cho, S. W.; Han, K.; Jeon, P.; Whang, C.-N.; Jeong, K.; Cho, K.; Yi, Y. *Appl. Phys. Lett.* **2008**, *93*, 043308.
(4) Greiner, M. T.; Helander, M. G.; Tang, W.-M.; Wang, Z.-B.; Qiu, J.; Lu, Z.-H. *Nat. Mater.* **2012**, *11*, 76−81.
(5) Meyer, J.; Hamwi, S.; Kröger, M.; Kowalsky, W.; Riedl, T.; Kahn, A. *Adv. Mater.* **2012**, *24*, 5408−5427.
(6) Lee, H.; Zhang, Y.; Zhang, L.; Mirabito, T.; Burnett, E. K.; Trahan, S.; Mohebbi, A. R.; Mannsfeld, S. C. B.; Wudl, F.; Briseno, A. L. *J. Mater. Chem. C* **2014**, *2*, 3361−3366.
(7) Ma, H.; Yip, H.-L.; Huang, F.; Jen, A. K.-Y. *Adv. Funct. Mater.* **2010**, *20*, 1371−1388.
(8) Qi, Y.; Sajoto, T.; Barlow, S.; Kim, E.-G.; Brédas, J.-L.; Marder, S. R.; Kahn, A. *J. Am. Chem. Soc.* **2009**, *131*, 12530−12531.
(9) Olthof, S.; Mehraeen, S.; Mohapatra, S. K.; Barlow, S.; Coropceanu, V.; Brédas, J.-L.; Marder, S. R.; Kahn, A. *Phys. Rev. Lett.* **2012**, *109*, 176601.
(10) Dai, A.; Zhou, Y.; Shu, A. L.; Mohapatra, S. K.; Wang, H.; Fuentes-Hernandez, C.; Zhang, Y.; Barlow, S.; Loo, Y.-L.; Marder, S. R.; Kippelen, B.; Kahn, A. *Adv. Funct. Mater.* **2014**, *24*, 2197−2204.
(11) Lloyd, M. T.; Peters, C. H.; Garcia, A.; Kauvar, I. V.; Berry, J. J.; Reese, M.; McGehee, M. D.; Ginley, D. S.; Olson, D. C. *Sol. Energy Mater. Sol. Cells* **2011**, *95*, 1382−1388.
(12) He, Z.; Zhong, C.; Su, S.; Xu, M.; Wu, H.; Cao, Y. *Nat. Photonics* **2012**, *6*, 591−595.
(13) Hoven, C. V.; Yang, R.; Garcia, A.; Crockett, V.; Heeger, A. J.; Bazan, G. C.; Nguyen, T.-Q. *Proc. Natl. Acad. Sci. U.S.A.* **2008**, *105*, 12730−12735.
(14) Seo, J. H.; Gutacker, A.; Sun, Y.; Wu, H.; Huang, F.; Cao, Y.; Scherf, U.; Heeger, A. J.; Bazan, G. C. *J. Am. Chem. Soc.* **2011**, *133*, 8416−8419.
(15) Ying, L.; Zalar, P.; Collins, S.; Chen, Z.; Mikhailovsky, A.; Nguyen, T.-Q.; Bazan, G. C. *Adv. Mater.* **2012**, *24*, 6496−6501.
(16) Zhou, H.; Zhang, Y.; Mai, C.-K.; Collins, S. D.; Nguyen, T.-Q.; Bazan, G. C.; Heeger, A. J. *Adv. Mater.* **2014**, *26*, 780−785.
(17) Seo, J. H.; Yang, R.; Brzezinski, J. Z.; Walker, B.; Bazan, G. C.; Nguyen, T.-Q. *Adv. Mater.* **2009**, *21*, 1006−1011.
(18) Seo, J. H.; Nguyen, T.-Q. *J. Am. Chem. Soc.* **2008**, *130*, 10042−10043.
(19) Hoven, C.; Yang, R.; Garcia, A.; Heeger, A. J.; Nguyen, T.-Q.; Bazan, G. C. *J. Am. Chem. Soc.* **2007**, *129*, 10976−10977.
(20) Garcia, A.; Bakus, R. C.; Zalar, P.; Hoven, C. V.; Brzezinski, J. Z.; Nguyen, T.-Q. *J. Am. Chem. Soc.* **2011**, *133*, 2492−2498.
(21) Page, Z. A.; Duzhko, V. V.; Emrick, T. *Macromolecules* **2013**, *46*, 344−351.
(22) Liu, F.; Page, Z. A.; Duzhko, V. V.; Russell, T. P.; Emrick, T. *Adv. Mater.* **2013**, *25*, 6868−6873.
(23) Fang, J.; Wallikewitz, B. H.; Gao, F.; Tu, G.; Müller, C.; Pace, G.; Friend, R. H.; Huck, W. T. S. *J. Am. Chem. Soc.* **2011**, *133*, 683−685.
(24) Duan, C.; Wang, L.; Zhang, K.; Guan, X.; Huang, F. *Adv. Mater.* **2011**, *23*, 1665−1669.
(25) Zhou, Y.; Fuentes-Hernandez, C.; Shim, J.; Meyer, J.; Giordano, A. J.; Li, H.; Winget, P.; Papadopoulos, T.; Cheun, H.; Kim, J.; Fenoll, M.; Dindar, A.; Haske, W.; Najafabadi, E.; Khan, T. M.; Sojoudi, H.; Barlow, S.; Graham, S.; Brédas, J.-L.; Marder, S. R.; Kahn, A.; Kippelen, B. *Science* **2012**, *336*, 327−332.
(26) Shim, J. W.; Zhou, Y.; Fuentes-Hernandez, C.; Dindar, A.; Guan, Z.; Cheun, H.; Kahn, A.; Kippelen, B. *Sol. Energy Mater. Sol. Cells* **2012**, *107*, 51−55.
(27) Khan, T. M.; Zhou, Y.; Dindar, A.; Shim, J. W.; Fuentes-Hernandez, C.; Kippelen, B. *ACS Appl. Mater. Interfaces* **2014**, *6*, 6202−6207.
(28) Zhang, Y.; Diao, Y.; Lee, H.; Mirabito, T. J.; Johnson, R. W.; Puodziukynaite, E.; John, J.; Carter, K. R.; Emrick, T.; Mannsfeld, S. C. B.; Briseno, A. L. *Nano Lett.* **2014**, *14*, 5547−5554.
(29) Frisch, M. J.; Trucks, G. W.; Schlegel, H. B.; Scuseria, G. E.; Robb, M. A.; Cheeseman, J. R.; Scalmani, G.; Barone, V.; Mennucci, B.; Petersson, G. A.; Nakatsuji, H.; Caricato, M.; Li, X.; Hratchian, H. P.; Izmaylov, A. F.; Bloino, J.; Zheng, G.; Sonnenberg, J. L.; Hada, M.; Ehara, M.; Toyota, K.; Fukuda, R.; Hasegawa, J.; Ishida, M.; Nakajima, T.; Honda, Y.; Kitao, O.; Nakai, H.; Vreven, T.; Montgomery, J. A., Jr.; Peralta, J. E. J.; Ogliaro, F.; Bearpark, M.; Heyd, J. J.; Brothers, E.; Kudin, K. N.; Staroverov, V. N.; Kobayashi, R.; Normand, J.; Raghavachari, K.; Rendell, A.; Burant, J. C.; Iyengar, S. S.; Tomasi, J.; Cossi, M.; Rega, N.; Millam, J. M.; Klene, M.; Knox, J. E.; Cross, J. B.; Bakken, V.; Adamo, C.; Jaramillo, J.; Gomperts, R.; Stratmann, R. E.; Yazyev, O.; Austin, A. J.; Cammi, R.; Pomelli, C.; Ochterski, J. W.; Martin, R. L.; Morokuma, K.; Zakrzewski, V. G.; Voth, G. A.; Salvador, P.; Dannenberg, J. J.; Dapprich, S.; Daniels, A. D.; Farkas, O.; Foresman, J. B.; Ortiz, J. V.; Cioslowski, J.; Fox, D. J. *Gaussian 09*, revision A.02; Gaussian, Inc.: Wallingford, CT, 2009.
(30) Becke, A. D. *J. Chem. Phys.* **1993**, *98*, 5648−5652.
(31) Lee, C.; Yang, W.; Parr, R. G. *Phys. Rev. B* **1988**, *37*, 785−789.
(32) Mendoza, S. M.; Arfaoui, I.; Zanarini, S.; Paolucci, F.; Rudolf, P. *Langmuir* **2007**, *23*, 582−588.
(33) Tour, J. M.; Jones, L., II; Pearson, D. L.; Lamba, J. J. S.; Burgin, T. P.; Whitesides, G. M.; Allara, D. L.; Parikh, A. N.; Atre, S. *J. Am. Chem. Soc.* **1995**, *117*, 9529−9534.
(34) Seah, M. P.; Spencer, S. J. *Surf. Interface Anal.* **2011**, *43*, 744−751.
(35) Lee, B. H.; Jung, I. H.; Woo, H. Y.; Shim, H.-K.; Kim, G.; Lee, K. *Adv. Funct. Mater.* **2014**, *24*, 1100−1108.
(36) Li, H.; Xu, Y.; Hoven, C. V.; Li, C.; Seo, J. H.; Bazan, G. C. *J. Am. Chem. Soc.* **2009**, *131*, 8903−8912.
(37) Kang, H.; Hong, S.; Lee, J.; Lee, K. *Adv. Mater.* **2012**, *24*, 3005−3009.
(38) Stöhr, J. *NEXAFS Spectroscopy*; Springer: Berlin; New York, 2003.
(39) DeLongchamp, D. M.; Kline, R. J.; Lin, E. K.; Fischer, D. A.; Richter, L. J.; Lucas, L. A.; Heeney, M.; McCulloch, I.; Northrup, J. E. *Adv. Mater.* **2007**, *19*, 833−837.
(40) Bierbaum, K.; Kinzler, M.; Woell, C.; Grunze, M.; Haehner, G.; Heid, S.; Effenberger, F. *Langmuir* **1995**, *11*, 512−518.
(41) Schultz, Z. D.; Feng, Z. V.; Biggin, M. E.; Gewirth, A. *J. Electrochem. Soc.* **2006**, *153*, C97−C107.
(42) Koch, N.; Vollmer, A.; Duhm, S.; Sakamoto, Y.; Suzuki, T. *Adv. Mater.* **2007**, *19*, 112−116.
(43) Wei, S.; Xia, J.; Dell, E. J.; Jiang, Y.; Song, R.; Lee, H.; Rodenbough, P.; Briseno, A. L.; Campos, L. M. *Angew. Chem., Int. Ed.* **2014**, *53*, 1832−1836.
(44) Duhm, S.; Heimel, G.; Salzmann, I.; Glowatzki, H.; Johnson, R. L.; Vollmer, A.; Rabe, J. P.; Koch, N. *Nat. Mater.* **2008**, *7*, 326−332.
(45) Ward, J. W.; Loth, M. A.; Kline, R. J.; Coll, M.; Ocal, C.; Anthony, J. E.; Jurchescu, O. D. *J. Mater. Chem.* **2012**, *22*, 19047−19053.
(46) Chen, W.; Huang, H.; Chen, S.; Huang, Y. L.; Gao, X. Y.; Wee, A. T. S. *Chem. Mater.* **2008**, *20*, 7017−7021.
(47) Schlesinger, R.; Xu, Y.; Hofmann, O. T.; Winkler, S.; Frisch, J.; Niederhausen, J.; Vollmer, A.; Blumstengel, S.; Henneberger, F.; Rinke, P.; Scheffler, M.; Koch, N. *Phys. Rev. B* **2013**, *87*, 155311.

(48) Schlaf, R.; Parkinson, B. A.; Lee, P. A.; Nebesny, K. W.; Armstrong, N. R. *J. Phys. Chem. B* **1999**, *103*, 2984−2992.
(49) Wang, H.; Amsalem, P.; Heimel, G.; Salzmann, I.; Koch, N.; Oehzelt, M. *Adv. Mater.* **2014**, *26*, 925−930.
(50) Yoshida, H. *J. Phys. Chem. C* **2014**, *118*, 24377−24382.
(51) Kumar, A.; Sista, S.; Yang, Y. *J. Appl. Phys.* **2009**, *105*, 094512.
(52) Perez, M. D.; Borek, C.; Forrest, S. R.; Thompson, M. E. *J. Am. Chem. Soc.* **2009**, *131*, 9281−9286.
(53) Graham, K. R.; Erwin, P.; Nordlund, D.; Vandewal, K.; Li, R.; Ndjawa, G. O. N.; Hoke, E. T.; Salleo, A.; Thompson, M. E.; McGehee, M. D.; Amassian, A. *Adv. Mater.* **2013**, *25*, 6076−6082.
(54) Matsushima, T.; Kinoshita, Y.; Murata, H. *Appl. Phys. Lett.* **2007**, *91*, 253504.
(55) Vasilopoulou, M.; Palilis, L. C.; Georgiadou, D. G.; Kennou, S.; Kostis, I.; Davazoglou, D.; Argitis, P. *Appl. Phys. Lett.* **2012**, *100*, 013311.